ACS APPLIED MATERIALS & INTERFACES

Letter

www.acsami.org

Intense Photocurrent from Mo-Doped TiO_2 Film with Depletion Layer Array

Sheng-Yun Luo,[†,‡] Bing-Xi Yan,[†] and Jie Shen*[,†]

[†]Department of Materials Science, Fudan University, Shanghai 200433, P. R. China

[‡]College of Science, Guizhou Minzu University, Guiyang 550025, P. R. China

Supporting Information

ABSTRACT: A novel bilayer structure of TiO_2 film was found capable of yielding fairly strong photocurrent under visible light. The base layer was lightly doped with Mo and then etched by reactive ion beam, and was finally covered by an undoped TiO_2 surface layer. Because of Fermi level drop at the interface of the trenches, such a deposition−etching−redeposition process implanted an array of depletion layer into TiO_2 film successfully. Microstructures, crystallite parameters, and the absorption property were investigated with scanning electron microscope, atomic force microscopy, X-ray diffraction, and ultraviolet−visible spectroscopy in order. Photocurrent density was collected on an electrochemical workstation under visible light. The results indicate that carrier collection probability near depletion layer was enhanced significantly owing to high parallel diffusivity. Under visible light, current density demonstrates a marked increase as etching depth grows. At an etching depth around 660 nm, photocurrent density achieved is 56 times larger than TiO_2 film. Depletion layer at vertical trench edges may have a much bigger universal value than anticipated for various doping cases of wide-bandgap films.

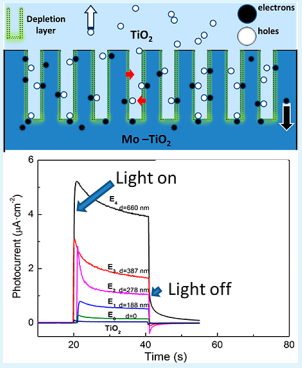

KEYWORDS: *depletion layer array, anisotropic transport, Mo doping, TiO_2 film, magnetron sputtering, reactive ion beam etching*

TiO_2 is a low-cost semiconductor with fairly good mechanical strength and chemical stability. Under visible light, TiO_2 provides photogenerated carriers and is widely used as photocatalyst, dye-sensitized solar cells, and water splitters for hydrogen production,[1−3] but the performance depends on the density of photogenerated carriers (electrons and holes). Nevertheless, a wide energy gap of 3.2 eV (anatase), which corresponds to an absorption edge of 380 nm, precludes most of these applications under visible light. To address this problem, band curtailing and transport acceleration are the two most used strategies. The first strategy could be realized by doping of cations, anions, or both of them.[4−8] Doping curtails band gap but will also raise defect density, boost up recombination rate, and then bring down carrier density. On the other hand, the second requires introduction of high mobility medium like nanotubes, nanowires, or graphene to speed up carrier transport and prevent recombination.[9−13] However, as film thickness shrinks smaller, the high cross-link ratio of these low-dimension media will also dramatically boost up recombination.

Although there are voluminous reports on optimized contents of countless dopants in various conditions, optimization of film structure has not aroused much concern until now. In a previous work, we proposed an approach to deposit a three-layer film with an ultrathin, heavily doped tunneling bottom, and confirmed this structure can raise current density of TiO_2 films by six times under visible light.[14] However, we also found that transport of carriers far from planar depletion layer cannot be accelerated effectively because high collection region near the depletion layer was rather thin due to a small perpendicular diffusivity, which is typical for all films materials featuring quantum confinement of electron movement along the perpendicular direction. To break this bottleneck, herein we wrinkled horizontal depletion layers and curved them deeply into the base layer by an alternative use of sputtering and reactive ions beam etching. In this new structure, perpendicular carrier diffusion in traditional bilayers was updated by parallel diffusion between depletion layers at trench edge. Because carrier movement along the parallel direction is not confined by film dimension, a marked increase of photocurrent was observed. In this work, we optimized trench depth and then focused exclusively on carrier transport mechanism.

All samples were deposited on titanium substrates by an RF magnetron sputtering machine (SY-300, Chinese academy of sciences) at room temperature in a background pressure of 2.0×10^{-3} Pa. Two targets were utilized for cosputtering: a TiO_2 ceramic target and the other embedded with a tiny Mo plate on the sputtering ring of TiO_2 ceramic target. Thicknesses of base layer (Mo-TiO_2) and surface layer (TiO_2) were obtained on an alpha-step device (ET 200, HITACHI) and confirmed by a scanning electron microscope (SEM, XL30FEG, Philips) as 1.4 and 0.3 μm, respectively. By modulating etching time and energy of ions beam, we gave an etching depth of 200 nm, 300 nm, 400 and 700 nm to Mo-doped bases of a 1.4 μm thickness, and then denote them by sample E_1, E_2, E_3, E_4, correspondingly. Another unetched bilayer sample is denoted by E_0 and

Received: April 14, 2014
Accepted: June 10, 2014
Published: June 10, 2014

   dx.doi.org/10.1021/am5021183 | ACS Appl. Mater. Interfaces 2014, 6, 8942−8946

used for comparison. All samples obtained were annealed in a furnace (SX2−8−10, Tianye) under 550 °C for 2 h to form ideal crystal phase. Structural characteristics and cross-sectional image of trench edge were studied by X-ray diffraction (XRD, pw1710X, Philips), an atomic force microscope microscopy (AFM, Park Scientific Instrument), and a scanning electron microscope (SEM, XL30FEG, Philips) in order. The absorption property of different structures was examined with ultraviolet−visible spectrometer (UV2300, Hitachi), whereas photocurrent density was collected on an electrochemical workstation under visible light (CHI660B, CH Instrument).

As shown in Figure 1a, adjacent trenches are separated by a 50 μm distance. Samples with four different trench depths were

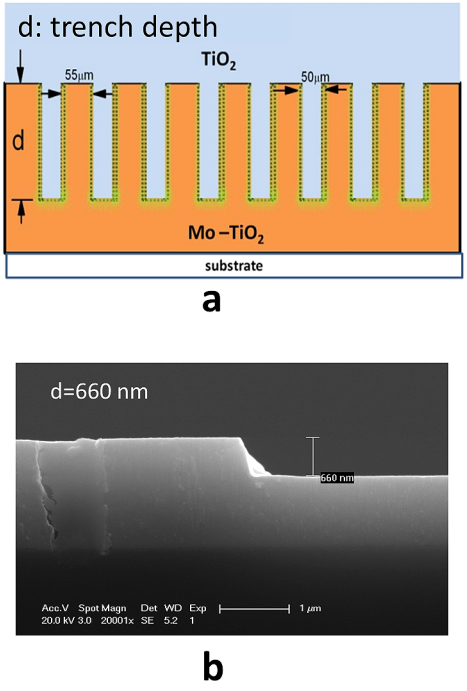

Figure 1. (a) Schematic illustration of trench arrays, and (b) step profile for sample E_4 with a depth around 660 nm.

fabricated in this work. Trench depth for sample E_1, E_2, and E_3 is 188, 278, and 387 nm. Figure 1b shows the cross-sectional image of sample E_4, which was given the largest etching depth around 660 nm. Considering the distance between two adjacent trenches (50 μm) is much larger than trench depth, even the largest depth (660 nm) can only bring a rather small area growth of total depletion layer (1.5%). For this reason, influence of area variation after etching is neglected here. A detailed profile of a trench edge for sample E_1 is given in the Supporting Information. Note that the actual etching depth at the trench edge is significantly larger than designed value because of ions beam scattering at the trench sidewalls. Due to this reason, to ensure the base is not etched through, practical etching depth should be smaller than the overall base thickness. Specifically, we suggest that the remaining base thickness after etching should be no less than 100 nm so as to protect the substrate against overetching effect at trench edge and prevent possible contaminant from the substrate.

Crystal structures of base and surface layer are studied by XRD in Figure 2a, where as expected only anatase was found. Data analysis from the software (Jade 5.0) suggests crystallite diameter decreases from 127.0 to 114.5 nm while lattice

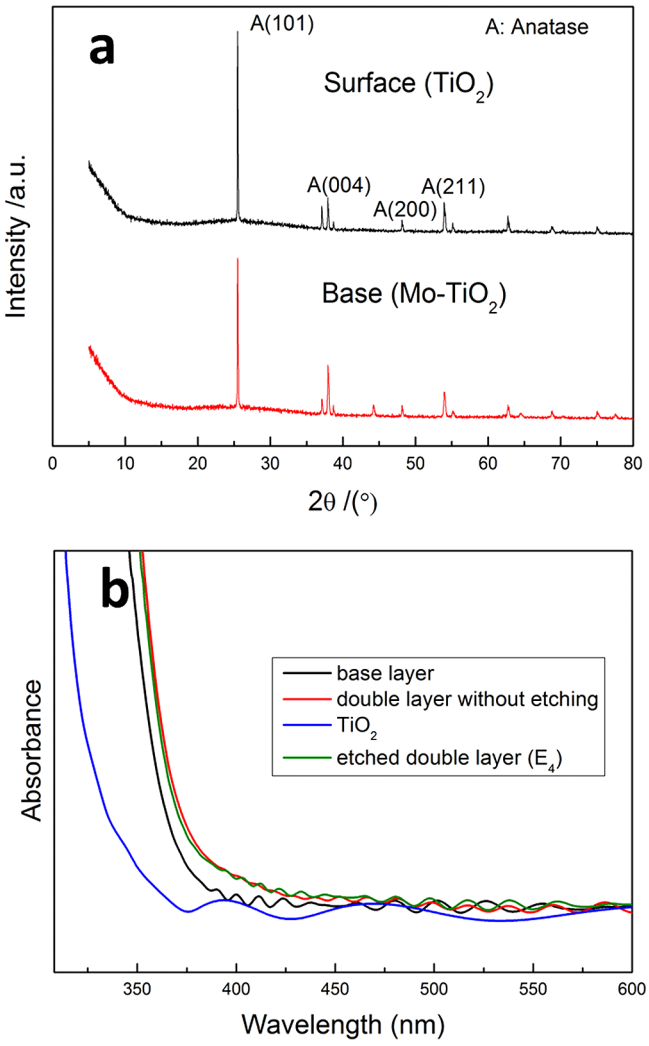

Figure 2. (a) XRD patterns of base and surface layer, and (b) absorption property of different structures under UV−vis light.

distortion grows from 0.0577 to 0.0640, corresponding to a diminishing main peak at 25.4° in the figure. Due to smaller lattice defects, recombination rate in the surface layer is much smaller the doped base. Following one of our previous works,[15] we gave an appropriate doping content of 0.6 at. % to base. Figure 2b indicates absorption property of ultraviolet−visible light. Because of n-doping and the formation of Mo−Ti−O bonds, Mo doping shifts the absorption edge of TiO_2 films from 360 to 380 nm.[16] Comparing the base layer and bilayer sample without etching, one can easily find another red-shift from 380 to 410 nm because of the Window Effect, which has been widely used in photovoltaic device design.[17] We found all bilayer samples have a highly overlapped absorption curve and difference between them is hardly visible. To make it clear, we picked out the data of E_4 as a representative of this group. From a comparison between it and the etched bilayer sample, we can see etching depth has very small impact over absorption property, which is an reasonable result considering the pattern period of the applied mask is fairly large (50 μm), so absorption property of all etched sample is still dictated by a traditional bilayer structure.

As shown in Figure 3, a significant increase of photocurrent density shows up after etching, and when compared to it the current of TiO_2 is almost undistinguishable. Quantitatively, if

dx.doi.org/10.1021/am5021183 | ACS Appl. Mater. Interfaces 2014, 6, 8942−8946

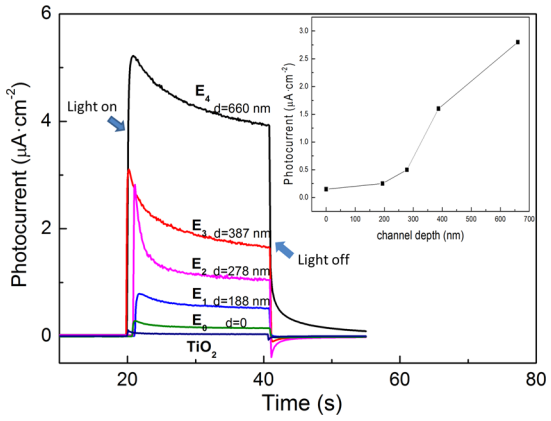

Figure 3. Photocurrent density of samples with different etching depths, the inset shows the correlation between etching depth and photocurrent density under visible light.

we denote current density of TiO_2 under visible light is 100%, then the bilayer sample (E_0) without etching is about 300%. As etching depth increases, current density bursts to 500% (E_1), 1000% (E_2), 3200% (E_3), and eventually 5600% (E_4). Considering there's no notable increase of light absorption or depletion layer area, such a dramatically increase substantiates carrier recombination was inhibited effectively in etched samples. Current increase at small etching depth is not so remarkable, perhaps due to carriers in shallow regions are already under positive influence of planar depletion layer. This is substantiated by the inset from the other aspect, where increase of current does not demonstrate any sign of saturation as depth grows. It seems that the deeper these trenches go, the stronger photocurrent would be. This confirms a large density of excessive carriers is accumulated at base bottom, which is in agreement with carrier density distribution along the perpendicular direction. Such bottom carriers give few contributions to photocurrent in a traditional bilayer structure like Figure 4a, mainly because they're too far away from depletion region at layer interface. For a structure shown in Figure 4b, however, holes are sucked into pluglike deep wells and transferred to film surface at a rather low recombination ratio because of a small defect density in the undoped surface layer.

Another key factor contributing to the sharp current increase is anisotropic transport property, that is, the parallel diffusivity of a film is usually much larger than perpendicular diffusivity. In a structure like Figure 4b, as the Fermi level of the base is higher than surface layer, a self-built electric field directed toward the surface layer is created within depletion layer at the interface. Consequently, under illumination of visible light, electrons within the depletion layer are swept into the bottom layer while holes are swept into the surface layer. Carrier transport within the depletion layer is very fast so recombination in this region could be neglected. However, the most important meaning of depletion layer is not the fast carrier transfer within depletion layer; instead, it is highlighted by the unique capability to raise the collection probability near the depletion region. Contribution of a hole−electron pair to the whole current density is dictated by the collection probability $P_{collect}$,[18] which is a function of position and decreases exponentially with the distance to the edge of depletion layer. In specific, $P_{collect} = \exp(-x/L_p)$, where x is the distance to junction edge, L_p is the diffusion length of minor

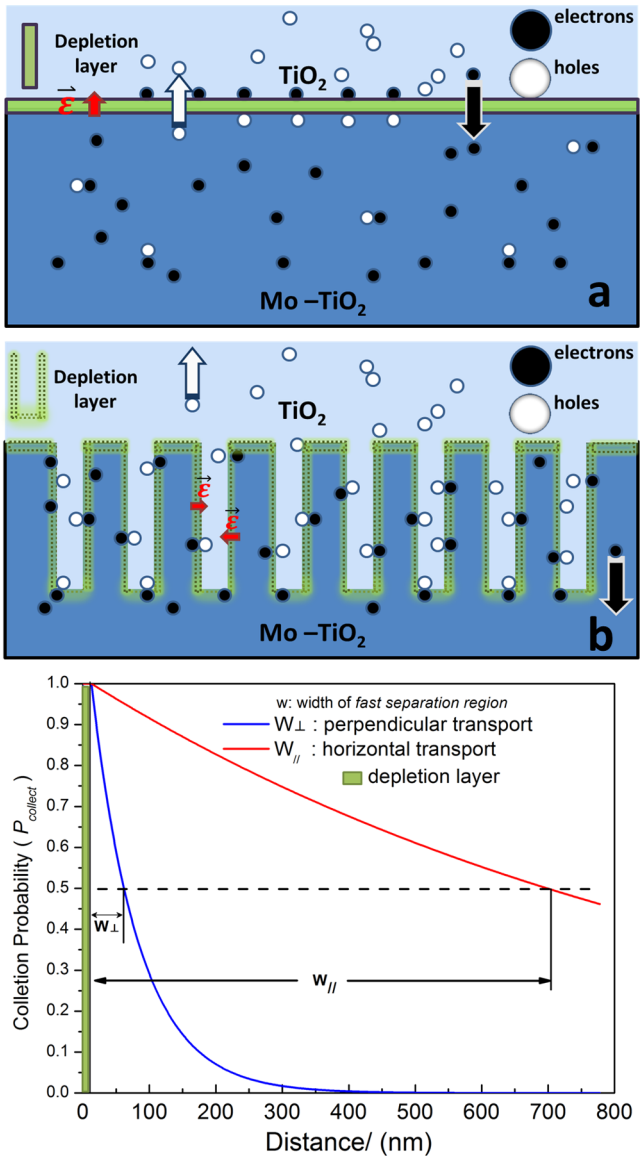

Figure 4. (a) Carriers transfer near a planar depletion layer, where the red arrow indicates direction and location of internal self-built field; (b) carriers transfer near a depletion layer array; (c) collection probability versus distance away from the edge of a depletion layer.

carriers (holes for n-type semiconductor here) and is proportional to the square root of diffusivity ($D^{1/2}$).[19] From the correlation above, it is easy to find the 50% collection ability corresponds to a distance of $0.7L_p$, where hereafter is taken as the edge of the fast separation region. If we denote the diffusion length in base and surface layer by L_{p1}, L_{p2}, respectively, then the overall width of this fast separation region is $W_{eff} = W + L_{p1} + L_{p2}$, and W is the small width of depletion layer and follows

$$W = \sqrt{\frac{2\varepsilon_s V_{bi}}{eN_d}} \quad (1)$$

where N_d is the donor concentration, ε_s is the dielectric constant in films, and V_{bi} is the barrier height at the surface/base interface that follows

dx.doi.org/10.1021/am5021183 | ACS Appl. Mater. Interfaces 2014, 6, 8942−8946

$$V_{bi} = \frac{kT}{e}\ln\left(\frac{n_2 N_{c1}}{n_1 N_{c2}}\right) \quad (2)$$

where n_1, n_2 is the electron concentration in surface and base layer, respectively. Because of the small dopant content, effective state density of the conduction band does not vary too much with or without doping. For a light doping case like here, even n increases by an order, the thickness of the depletion layer at the layer interface is still very small because of a small barrier height V_{bi} (0.06 V). Specifically, when N_d in the base layer is $6 \times 10^{19}/cm^3$ (0.6 at %), depletion layer will has a width of 5.1 nm and much smaller compared to diffusion length, as confirmed in following calculation. Owing to a small effective mass, carrier diffusivity (D) along the parallel (horizontal) direction is much larger than the perpendicular one,[20−23] which gives rise to higher diffusion length as $L=(D\tau)^{1/2}$, with D is the diffusivity and τ is average lifetime of carriers. This important principle could also be obtained by comparing parallel and perpendicular carrier mobility (μ) given the Einstein relationship $D = \mu kT/e$, where k is the Boltzmann constant, T is the temperature, e is the electron charge. For anatase film, perpendicular diffusivity D is as small as 0.0025 cm^2/s that corresponds to a mobility value below 0.1 $cm^2/V\cdot s$.[20,21] As the typical value τ for anatase annealed at 550 °C is 20 ns,[22] the perpendicular diffusion length (L_{per}) is around 70.7 nm ($W_{\perp}$), as indicated by Figure 4a. Most carriers that are 49.5 nm (0.7 L_{per}) away from the depletion edge will recombine before reaching the depletion layer. Along the parallel direction, however, the fast separation region is significantly broadened owing to a much larger parallel (horizontal) diffusivity of 0.5 cm^2/s.[20,23] In this case, width of parallel fast separation regions ($W_{//}$) increased to 700 nm and is 14 times larger the perpendicular one. As shown in Figure 4 (c), by altering the horizontal (parallel) depletion layer to a perpendicular array, more carriers in the etched base now can benefit from high collection possibility. After these discussions, we need to point out that a smaller trench distance may increase the total area of depletion layer a step further. In principle, if trench density approaches a limit value of $2W$ (W is the width of fast separation region and equals $0.7L$ as discussed above), collection probability of the whole base could be higher than 50%, and then very low recombination rate could be anticipated. Another noteworthy point lies in that the value of this structure is perhaps not confined within certain dopants; in contrast, it may also raise current density by an order or more for other dopants in various wide-bandgap materials.

In conclusion, vertical trench arrays with 50 μm distance were curved on Mo-doped TiO_2 base by reactive ion beam etching. Because of high parallel diffusivity in film materials, the depletion layer resulting from the Fermi level drop at the interface gives rise to many wide fast separation regions near trench edges, where carrier recombination is effectively reduced. Holes reaching depletion layer edge are transported to film surface at a quite low recombination rate because of the low defect density in the top layer. With trench depth increasing to 188 nm, 278 and 387 nm in order, current density indicates a growth of 500, 1000, and 3200% under visible light (compared to TiO_2 films of equal thickness). Specifically, when the etching depth reached 660 nm, current density demonstrated a sharp increase of 5600%, which is more notable than many other doping studies based on anions, cations, or nanowires.

■ ASSOCIATED CONTENT

Supporting Information

Experimental parameters and detailed fabrication steps are included in the Supporting Information, where an image of trench array and an AFM profile of trench edge could also be found. This material is available free of charge via the Internet at http://pubs.acs.org/.

■ AUTHOR INFORMATION

Corresponding Author

*E-mail: shenjie@fudan.edu.cn.

Notes

The authors declare no competing financial interest.

■ ACKNOWLEDGMENTS

This work is supported by the National Key Basic Research Program of China (973) (2012CB934303), the joint fund launched by the department of science and technology of Guizhou province & Guizhou Minzu University (LKM [2012] 24), Guiyang Science & Technology Department ([2012205] 6-12).

■ REFERENCES

(1) Karakitsou, K. E.; Verykios, X. E. Effects of Altervalent Cation Doping of Titania on its Performance as a Photocatalyst for Water Cleavage. *J. Phys. Chem.* **1993**, *97*, 1184−1189.

(2) Song, W. J.; Luo, H. L.; Hanson, K.; Concepcion, J. J.; Brennaman, M. K.; Meyer, T. J. Visualization of Cation Diffusion at the TiO_2 Interface in Dye Sensitized Photoelectrosynthesis Cells (DSPEC). *Energy Environ. Sci.* **2013**, *6*, 1240−1248.

(3) Singh, D.; Yadav, P.; Singh, N. J.; Kant, C.; Kumar, M.; Sharma, S. D.; Saini, K. K. Dielectric Properties of Fe-doped TiO_2 Nanoparticles Synthesised by Sol−gel Route. *Exp. Nanosci.* **2013**, *8*, 171−183.

(4) Likodimos, V.; Han, C.; Pelaez, M.; Kontos, A. G.; Liu, G.; Zhu, D.; Liao, S.; Cruz, A. A.; O'Shea, K.; Dunlop, P. M.; Byrne, J. A.; Dionysiou, D.; Falaras, P. Anion-Doped TiO_2 Nanocatalysts for Water Purification under Visible Light. *Indus. & Eng. Chem. Res.* **2013**, *52*, 13957−13964.

(5) Fittipaldi, M.; Gatteschi, D.; Fornasiero, P. The Power of EPR Techniques in Revealing Active Sites in Heterogeneous Photocatalysis: The Case of Anion Doped TiO_2. *Catal. Today* **2013**, *206*, 2−11.

(6) Cong, Y.; Zhang, J.; Chen, F.; He, D. Preparation, Photocatalytic Activity, and Mechanism of Nano-TiO_2 Co-doped with Nitrogen and Iron (III). *J. Phys. Chem. C* **2007**, *111*, 10618−10623.

(7) Jaćimović, J.; Gaál, R.; Magrez, A.; Forró, L.; Regmi, M.; Gxula, E. Electrical Property Measurements of Cr-N Codoped TiO_2 Epitaxial Thin Films Grown by Pulsed Laser Deposition. *Appl. Phys. Lett.* **2013**, *102*, 172108.

(8) Zhang, P.; Yin, S.; Sekino, T.; Lee, S. W.; Sato, T. Nb and N Co-doped TiO_2 for a High-performance deNO_x Photocatalyst under Visible LED Light Irradiation. *Res. Chem. Intermed.* **2013**, *39*, 1509−1515.

(9) Bavykin, D. V.; Passoni, L.; Walsh, F. C. Hierarchical Tube-in-tube Structures Prepared by Electrophoretic Deposition of Nanostructured Titanates into a TiO_2 Nanotube Array. *Chem. Commun.* **2013**, *49*, 7007−7009.

(10) Farsinezhad, S.; Dalrymple, A. N.; Shankar, K. Toward Single-step Anodic Fabrication of Monodisperse TiO_2 Nanotube Arrays on Non-native Substrates. *Phys. Status Solidi (a)* **2014**, *10*, 1862−6319.

(11) Wang, G. M.; Wang, H. Y.; Ling, Y. C.; Tang, Y. C.; Yang, X. Y.; Fitzmorris, R. C.; Wang, C. C.; Zhang, J. Z.; Li, Y. Hydrogen-treated TiO_2 Nanowire Arrays for Photoelectrochemical Water Splitting. *Nano Lett.* **2011**, *11*, 3026−3033.

(12) Hwang, Y. J.; Hahn, C.; Liu, B.; Yang, P. D. Photoelectrochemical Properties of TiO_2 Nanowire Arrays: a Study of the

Dependence on Length and Atomic Layer Deposition Coating. *ACS Nano* **2012**, *6*, 5060−5069.
(13) Zhang, X. Y.; Li, H. P.; Cui, X. L.; Lin, Y. H. Graphene/TiO_2 Nanocomposites: Synthesis, Characterization and Application in Hydrogen Evolution from Water Photocatalytic Splitting. *J. Mater. Chem.* **2010**, *20*, 2801−2806.
(14) Yan, B. X.; Luo, S. Y.; Mao, X. G.; Shen, J.; Zhou, Q. F. Unusual Photoelectric Behaviors of Mo-doped TiO_2 Multilayer Thin Films Prepared by RF Magnetron Co-sputtering: Effect of Barrier Tunneling on Internal Charge Transfer. *Appl. Phys. A: Mater. Sci. Process.* **2013**, *110*, 129−135.
(15) Yan, B. X.; Luo, S. Y.; Shen, J. Photoelectric Properties of Mo doped TiO_2 Thin Films Deposited by DC Reactive Magnetron Sputtering. *Acta Phys.-Chim. Sin.* **2012**, *28*, 381−386.
(16) Pan, S. S.; Zhang, Y. X.; Teng, X. M.; Li, G. H.; Li, L. Optical properties of nitrogen-doped SnO_2 films: Effect of the electronegativity on refractive index and band gap. *J. Appl. Phys.* **2008**, *103*, 093103.
(17) Chen, Z. M.; Wang, J. N.; Mei, X. Y.; Kong, G. L. a-Si: H/a-C: H Amorphous Semiconductor Superlattices. *Solid State Commun.* **1986**, *58*, 379−384.
(18) Honsberg, C.; Bowden, S. http://www.pveducation.org/pvcdrom/solar-cell-operation/collection-probability (accessed April 2, 2014).
(19) Neamen, D. A. *Semiconductor Physics and Devices: Basic Principles*, third ed.; Publishing House of Electronics Industry, Beijing; p 162.
(20) Warman, J. M.; de Haas, M. P.; Picbat, P.; Serpone, N. Effect of Isopropyl Alcohol on the Surface Localization and Recombination of Conduction-band electrons in Degussa P25 TiO_2: a Pulse-Radiolysis Time-Resolved Microwave Conductivity Study. *J. Phys. Chem.* **1991**, *95*, 8858−8861.
(21) Tang, H.; Prasad, K.; Sanjines, R.; Schmid, P. E.; Levy, F. Electrical and Optical Properties of TiO_2 Anatase Thin Films. *J. Appl. Phys.* **1994**, *75*, 2042−2047.
(22) Colbeau-Justin, C.; Kunst, M.; Huguenin, D. Structural Influence on Charge-Carrier Lifetimes in TiO_2 Powders Studied by Microwave Absorption. *J. Mater. Sci.* **2003**, *38*, 2429−2437.
(23) Martin, S. T.; Herrmann, H.; Choi, W.; Hoffmann, M. R. Time-Resolved Microwave Conductivity. *J. Chem. Soc. Faraday Trans.* **1994**, *90*, 3315−3322.